J. Astrophys. Astr. (2023) 44:61
https://doi.org/10.1007/s12036-023-09955-7

STAR FORMATION

Photometric and kinematic studies of open cluster NGC 1027

APARA TRIPATHI[1,*], NEELAM PANWAR[2], SAURABH SHARMA[2], BRIJESH KUMAR[2] and SHANTANU RASTOGI[1]

[1]DDU Gorakhpur University, Gorakhpur 273009, India.
[2]Aryabhatta Research Institute of Observational Sciences, Nainital 263001, India.
*Corresponding author. E-mail: aparatrip@gmail.com

MS received 17 November 2022; accepted 30 March 2023

Abstract. We present photometric and kinematic analyses of an intermediate-age open cluster NGC 1027 using $UBV(RI)_c$ and Gaia Early Data Release 3 (EDR3) data. Structural and fundamental parameters, such as cluster center, cluster extent, reddening, age and distance are estimated in this study. Cluster center is found about 4 arcmin away from the center reported earlier. Radius has been estimated to be about 8.00 arcmin (2.65 pc). Using proper motion Gaia EDR3 data, membership probabilities have been derived for the stars in the region of cluster radius. We found mean proper motion of the cluster to be $\sim(-0.84, 2.04)$ mas yr^{-1} in (RA, DEC). We found 217 most probable ($P_\mu > 70\%$) cluster members with mean parallax 0.892 ± 0.088 mas. Out of these, 160 members have counterparts in our optical observations. Few stars having $P_\mu > 70\%$, are found out of the cluster radius showing imprints of dynamical evolution. The color–color and color–magnitude diagrams for the cluster members found within 8.00 arcmin have been constructed using $UBV(RI)_c$ photometry and Gaia EDR3 data. This yields a reddening $E(B-V) \sim 0.36$ mag, age $\sim$130 Myr and distance $\sim$1.14 kpc. The mass function slope in the cluster region is $\Gamma \sim -1.46 \pm 0.15$, which is similar to other Galactic open clusters. The dynamical study shows lack of faint stars in its inner region leading to mass segregation effect. A comparison of dynamical age with cluster age indicates that NGC 1027 is a dynamically relaxed cluster suggesting that mass segregation may be imprint of its dynamical relaxation.

Keyword. Star: open star cluster: color–magnitude diagrams: individual: NGC 1027—mass function—mass segregation.

1. Introduction

Stars in the Galaxy often form in star clusters. They contain stars of diverse mass range that are gravitationally bound and presumably formed from the same molecular material, at same time and located at the same distance and move together (Harris & Pudritz 1994; Friel 1995; Bate *et al.* 2003; Carraro & Costa 2007; Cantat-Gaudin & Anders 2020; Pang *et al.* 2020). Observations suggest that the age of Galactic star clusters range from a few Myr to few Gyr, indicating that they have been forming all along the life of our Galaxy. External forces of interaction with the galactic tidal field and two body relaxation effect changes the structure of open cluster probing them to be good targets to investigate astrophysical processes involved in formation and evolution of stars and Galaxies (Miholics *et al.* 2014; Tripathi *et al.* 2014; Tang *et al.* 2019).

Intermediate-age open clusters (OCs) are located in the disc of the Galaxy. Study of these type of OCs play a crucial role in advancing our understanding of the physical processes involved, such as change in its structure, mass function, mass segregation and develop the mechanism that govern their evolution by time. They probe the dynamical and chemical evolutions of the galactic disc in age and metallicity. Their study also improvise important constraints for the evolutionary astrophysical models (Sagar *et al.* 1986; Phelps & Janes 1994; Lada & Lada 2003; Chen *et al.* 2003; Joshi *et al.* 2016; Castro-Ginard *et al.* 2018; Angelo *et al.* 2019; Cantat-Gaudin & Anders 2020).

NGC 1027 also known as Melotte 16, Collinder 30, OCL 357, MWSC 225 open star cluster, is located in the eastern part of Cassiopeia constellation near the northern celestial pole, adjacent to two prominent nebulae,

This article is part of the Special Issue on "Star formation studies in the context of NIR instruments on 3.6m DOT".

Published online: 20 June 2023

Table 1. Parameters listed in WEBDA for cluster NGC 1027.

Cluster parameter	Values
Trumpler class	IIIp
RA (J2000)	02:42:40
Dec (J2000)	+61:35:42
Longitude (l/deg)	135.758
Latitude (b/deg)	1.525
Distance (d/pc)	722
Reddening ($E(B-V)$/mag)	0.325
Age (log(t/yr))	8.203

the Heart (IC 1805) and Soul Nebulae (IC 1848). However, NGC 1027 is not physically associated with these two nebulae as they are more distant ($d \sim 2.1$ kpc; Chauhan *et al.* 2011; Panwar *et al.* 2017) compared to the NGC 1027 ($d \sim 1$ kpc; Maciejewski & Niedzielski 2007). Some basic parameters of the cluster as reported in WEBDA, a site devoted to stellar clusters in the Galaxy and the magellanic clouds are listed in Table 1. Ruprecht (1966) considered this cluster as class III 2 p, i.e., a less populated open cluster with noticeable concentration and a medium range in magnitude of the stars (Trumpler 1930).

Based on the wide-field BV CCD photometric survey, Maciejewski & Niedzielski (2007) reported basic parameters of 42 open clusters (OCs) including NGC 1027. They estimated reddening $E(B-V) \sim 0.41 \pm 0.12$ mag, log age ~ 8.4 and distance $\sim$1.03 kpc for NGC 1027. Liu & Pang (2019) cataloged 2443 cluster candidates using Star cluster Hunting Pipeline (SHiP) and classified NGC 1027 as an old class III star cluster with a prominent MS turn-off in the color–magnitude diagram (CMD). He suggested for re-investigation of class III star cluster candidates.

Photometric studies of OCs are found to be fundamental tools to determine their structural parameters. These parameters play an important role towards understanding galactic structure and evolution. However, most of the OCs are affected by field star contamination. Therefore, finding out member stars of the cluster becomes necessary to look into the cluster properties (Carraro *et al.* 2008; Kharchenko *et al.* 2013; Cantat-Gaudin *et al.* 2018). Several methods by different researches have been suggested to determine membership of cluster stars (Medhi & Tamura 2013; Gao 2014). Proper motion diagram is a reliable tool to identify cluster members on the basis of astrometric precision and membership determination on kinematic method (e.g., Cantat-Gaudin *et al.* 2018; Castro-Ginard *et al.* 2018, 2020; Bisht *et al.* 2019; Cantat-Gaudin & Anders 2019; Joshi *et al.* 2020). This precise learning of cluster membership gives information about distribution of stellar mass in the OCs and throw light on dynamic evolution of star clusters. Numerous research studies have obtained present-day MF for a number of OCs (Dib *et al.* 2017; Bostancı *et al.* 2018; Joshi *et al.* 2020), yet, it is still not clear weather initial mass function (IMF) is universal in time and space or depends upon different star-forming conditions (Elmegreen 2000; Kroupa 2002; Bastian *et al.* 2010). Study of the distribution of low and high mass stars towards the cluster region provides a clue to the mass segregation in OCs.

In the present work, $UBVR_cI_c$ photometry for NGC 1027 has been done for the first time. We investigated the spatial structure, basic parameters, extent, reddening and age to understand the dynamical evolution of the cluster using the kinematic Gaia EDR3 data. Our high quality CCD photometry data go down to $V \sim 22$ mag. We estimate membership probabilities of stars in the cluster NGC 1027 down to $G \sim 20$ mag. The high probability members are utilized to examine mass function and mass segregation in the cluster NGC 1027.

The organization of the paper is as follows. Section 2 provides a brief description of the observations, data reduction procedures and astrometric calibration. Results and analysis including radial density profile, kinematic members, reddening, CMDs, age and distance to the cluster is discussed in Section 3. We discuss the results including a discussion on the presence of kinematic members beyond the cluster radius in Section 4 and Section 5 summarizes the results.

2. Observations and data reduction

2.1 $UBVR_cI_c$ photometric observations

The CCD $UBVR_cI_c$ data used in this study is taken using 104-cm Sampurnanand Telescope (ST) of the Aryabhatta Research Institute of Observational Sciences (ARIES), Nainital. The telescope covers about 13×13 arcmin^2 on the sky. To improve signal-to-noise ratio, binned mode of 2×2 pixel is used during the observations. The observing log is given in Table 2. Several number of bias and twilight flat-field frames were taken in all the filters along with multiple short and long exposure frames of the target and standard fields. To calibrate the magnitude of stars in cluster field, standard field SA 104 of Landolt (1992) is observed. Basic steps are performed using the standard tasks within the IRAF data reduction package for pre-processing of data

Table 2. Description of the optical observation for NGC 1027 and standard field, with dates and exposure times for each passband.

Cluster / standard field	Date	Filter	Exp. (s) × no. of frames
NGC 1027	24/25 Jan 2006	*V*	120 × 3
		B	180 × 3
		I	60 × 2
		R	60 × 2300 × 3
		U	300 × 2
	24 Dec 2005	*V*	900 × 2
		B	1200 × 3
		I	240 × 3
		R	300 × 3
		U	1800 × 2
SA 104	24/25 Jan 2006	*V*	130 × 5180 × 1
		B	200 × 5240 × 1
		I	60 × 7
		R	100 × 5120 × 2
		U	300 × 4240 × 1

frames, which includes bias subtraction, flat fielding and cosmic ray removal.

Airmass covers range of 1.2 to 1.3 for Landolt (1992) standards. Nine standard stars of Landolt (1992) is taken from the observed field of SA 104. The mean FWHM varies about 2 arcsec over the entire observation period.

2.2 *Photometric and astrometric calibration*

Photometry of bias-subtracted and flat-field corrected CCD frames is carried out using DAOPHOT-II software (Stetson 1987, 2000). Quantitative values for the brightness of stars are obtained by aperture photometry and profile fitting photometry.

Measurements of bright stars, which are saturated in deep exposure frames have been taken from short-exposure frames. For translating the observed aperture magnitudes to the standard magnitudes, least-square linear regressions outlined by Stetson (2000), are fitted. The instrumental magnitude calibration equations are as follows:

$$v = V + 4.22 \pm 0.01 - (0.04 \pm 0.01)(B - V) + (0.21 \pm 0.01)X,$$

$$b = B + 4.65 \pm 0.01 - (0.06 \pm 0.01)(B - V) + (0.33 \pm 0.01)X,$$

$$i = I_c + 4.67 \pm 0.01 - (0.02 \pm 0.01)(V - I_c) + (0.09 \pm 0.01)X,$$

$$r = R_c + 4.13 \pm 0.01 - (0.04 \pm 0.01)(V - R_c) + (0.16 \pm 0.01)X,$$

$$u = U + 6.86 \pm 0.01 - (0.03 \pm 0.01)(U - B) + (0.61 \pm 0.01)X.$$

Here, V, B, R_c, I_c and U are standard magnitudes and v, b, i, r, u represent instrumental aperture magnitudes normalized for 1 s of exposure time and X is the airmass. Second order color correction terms are small when compared to the other photometric data reduction error. Hence, they are ignored. Zero-points for local standards are evaluated accounting the aperture growth curve, difference in exposure times and atmospheric extinction. Errors in zero-points and color coefficients are ∼0.01 mag. A final catalog of stellar objects identified in atleast two filters were obtained with shape-defining parameters 0.2 ≤ sharpness <1.0 and goodness of fit estimator $\chi < 5$. The accuracy of the morphology and position of the cluster features in CMDs depend on the variation of photometric errors with magnitudes. Photometric errors are approximated to be related with the signal-to-noise ratio of the source.

The internal errors as derived from DAOPHOT in U, B, V, R_c and I_c are plotted against V mag in Figure 1. This shows that the photometric error is <0.01 mag in B up to $V \sim 17$ mag; <0.01 mag in V, R and I up to $V \sim 18$ mag; and for U-band it is <0.01 mag up to $V \sim 16$ mag.

Astrometric solutions are used to get celestial coordinates of all the stars in J2000.0. We use the CCMAP and CCTRAN tasks of IRAF to obtain the celestial coordinates of the detected stars. The sources detected in different wavebands are band merged using a matching radius of ∼2 arcsec. In total, 5913 stars are detected in all five bands. To determine the completeness of our $UBVR_cI_c$ data, we used the magnitude histograms (Panwar *et al.* 2017). We found that completeness of the data in V, B, I_c, R_c and U band is limited to about 20, 20.5, 18, 19 and 20 mag, respectively.

2.3 *Kinematic data from Gaia EDR3*

The Early Gaia Data Release 3 (Gaia Collaboration 2020) came to public in the year 2020. This data consists of five parametric astrometric solutions, which include positions on the sky (α, δ) parallaxes and proper motion (PM) $(\mu_\alpha \cos\delta, \mu\delta)$ with a limiting magnitude of $G \sim 21$ mag. The Gaia EDR3 data are comparatively more accurate than the Second Gaia Data Release (Gaia Collaboration *et al.* 2018).

For analysis, we have cross-matched the optical CCD data with Gaia EDR3 (Gaia Collaboration 2020). Parallax uncertainties are in the range up to 0.02–0.03 milliarcsec (mas) for sources at $G \leq 15$ mag and 0.07

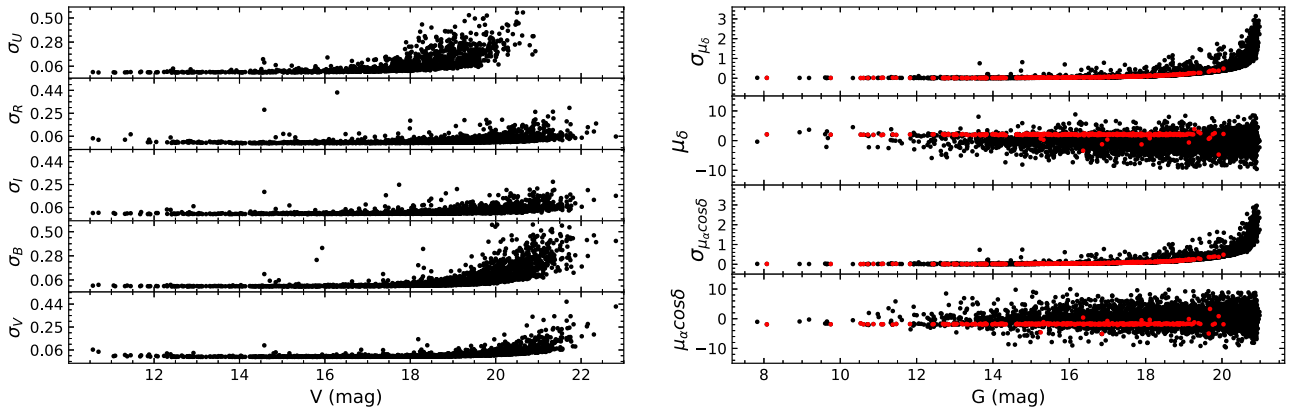

Figure 1. Left panel shows photometric errors corresponding to the brightness measurement at U, B, V, R_c and I_c against V-band brightness. Errors on the y-axis represent the internal error as estimated by DAOPHOT routine. Right panel shows the plot of proper motions in both RA and declination directions and their errors versus G magnitude. Blue symbol represents stars having membership probability >70%.

mas for sources at $G \sim 17$ mag. The uncertainties in the respective proper motion components are up to 0.01–0.02 mas yr^{-1} for $G \leq 15$ mag, 0.05 mas yr^{-1} for ∼20 mag. Proper motion and their corresponding errors are plotted against G mag in right panel of Figure 1.

3. Data analysis and results

3.1 *Cluster center and radial density profile*

To obtain the cluster parameters, first, we estimate the cluster center using the Python Kernel density estimation (KDE). For this, we use the Gaia EDR3 data for the sources with G-band magnitude uncertainty ≤0.1 mag within 40 arcmin radius around the cluster center as mentioned in the WEBDA. Our analysis shows the cluster center at α, δ (∼02:42:43.9, +61:39:34; about 4 arcmin away from the center mentioned in WEBDA). Cluster radius (r_{cl}) is taken as the distance from cluster center to where the average cluster contribution becomes negligible with respect to the background stellar field.

Cluster radius as well as extent of field-star contamination is estimated using spatial surface density profile of stars. For quantitative estimation of the cluster size, we have taken the concentric circular regions around the estimated cluster center. Star counts within each annular ring of width about 36 arcsec is divided by the respective areas of the annular rings to obtain the number density. To estimate the structural parameters (King 1962), surface density profile is fitted to the radial distribution of stars. The fit is done using a non-linear least squares fit routine, which uses the errors as weight. The radial density profile can be represented by:

$$f(r) = \frac{f_0}{1 + (\frac{r}{r_c})^2} + f_b, \quad (1)$$

where f_0 is the central density region, r_c is the core radius of the cluster and f_b is the background density.

The best fit solution along with uncertainties for density distribution is shown in Figure 2. The radial density profile of the cluster NGC 1027 decreases and flattens around 8 arcmin. Therefore, for further analyses, we have considered the cluster radius as 8 arcmin, which is <10.3 arcmin, the value reported before by Maciejewski & Niedzielski (2007). For NGC 1027, $f_0 = 2.2$ stars arcmin^{-2}, $r_c = 2.4$ arcmin and $f_b = 2.3$ stars arcmin^{-2}.

3.2 *Kinematic members of the cluster NGC 1027 with Gaia EDR3*

We used Gaia EDR3 data for the sources within the cluster region to select the cluster members and to determine mean proper motion of cluster NGC 1027 (radius ≤8 arcmin). We use the proper motion in RA ($\mu_\alpha^\star$) and proper motion in declination (μ_δ) for the stars within the cluster radius to generate the vector point diagram (VPD), where $\mu_\alpha^\star \equiv \mu_\alpha \cos(\delta)$. We consider only those sources with proper motion uncertainty <0.5 mas yr^{-1} and G-band magnitude uncertainty <0.1 mag. The VPD for those sources is shown in Figure 3. The over-density of sources can be easily noticed in Figure 3. The proper motion of the stars in the cluster region peaks at $(\mu_\alpha^\star, \mu_\delta) \sim (-0.84, 2.04)$ mas yr^{-1}.

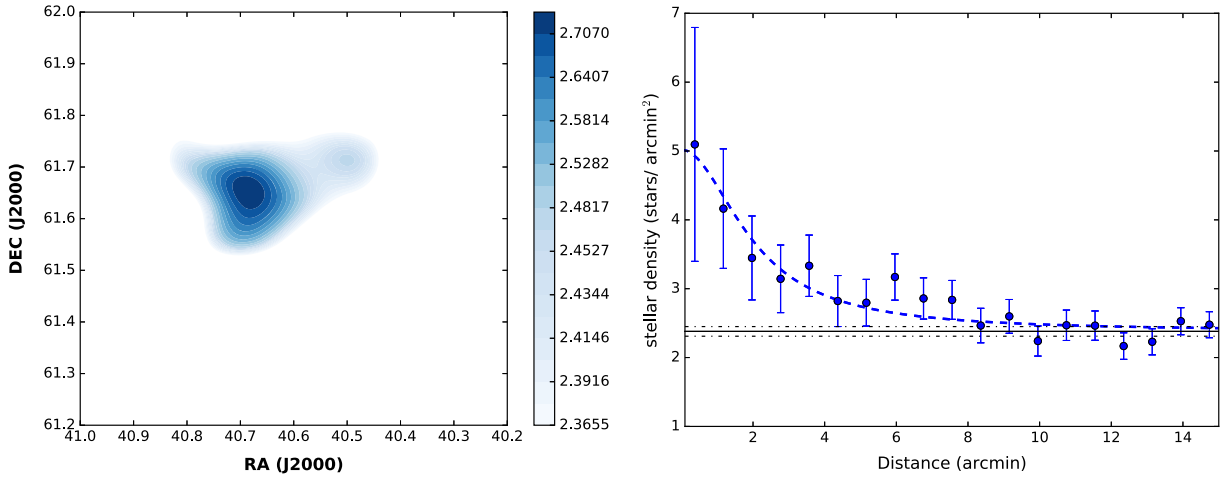

Figure 2. Left panel: The color maps are two-dimensional kernel density estimations (KDEs) of the spatial distribution of the bright GAIA EDR3 sources ($G \leq 17$ mag). Right panel: The radial density profile for the bright stars in the region. Dashed curve represents the least-square fit of the King (1962) profile to the observed data points. The error bars represent $\pm\sqrt{N}$ errors. The black line indicates the density of field stars.

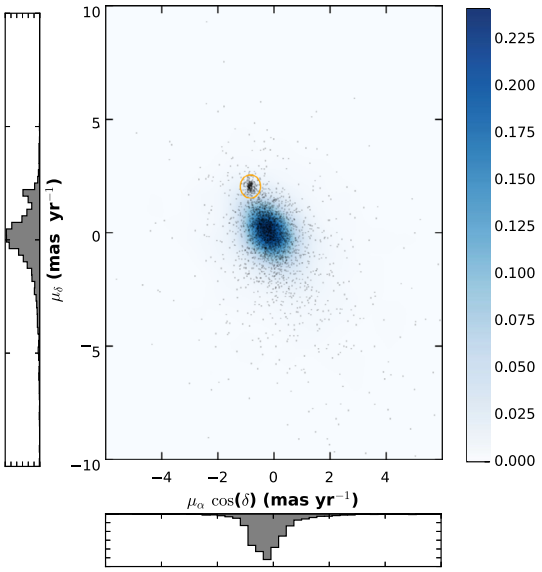

Figure 3. Proper motion vector-point diagram for the Gaia sources located within the cluster radius. Blue color bar shows the distribution of the proper motions for the stars in the control field of the similar area.

A circular area of radius 0.7 mas yr^{-1} around the peak of the over-density in the VPD is used to select the probable cluster members, and the remaining sources in the VPD are considered as field stars. To determine the membership probability of the stars in the cluster region, we use the approach discussed in Pandey *et al.* (2020). Assuming a distance of ∼1.14 kpc (see Section 3.4) and a radial velocity dispersion of 1 km s^{-1} for open clusters (Girard *et al.* 1989), a dispersion (σ_c) of ∼0.19 mas yr^{-1} in the PMs of the cluster can be obtained. We obtain $\mu_{xf} = -0.08$ mas yr^{-1}, $\mu_{yf} = -0.33$ mas yr^{-1}, $\sigma_{xf} = 1.05$ mas yr^{-1} and $\sigma_{yf} = 2.02$ mas yr^{-1} for the probable field members. These values are further used to construct the frequency distributions of the cluster stars (ϕ_c^v) and field stars (ϕ_f^v) by using the equation given in Yadav *et al.* (2013) and then, the value of membership probability for the ith star is calculated using the equation given below:

$$P_\mu(i) = \frac{n_c \times \phi_c^v(i)}{n_c \times \phi_c^v(i) + n_f \times \phi_f^v(i)}, \tag{2}$$

where n_c and n_f are the normalized number of probable cluster members and field members, respectively. In Figure 4 (upper panel), we have plotted the estimated membership probability for all the Gaia sources within the cluster radius as a function of G-band magnitude as blue dots. Gaia sources with high membership probability ($P_\mu > 70\%$) are shown with red circles. Two hundred and seventeen stars has been found with $P_\mu > 70\%$. There is a clear separation between the cluster members and field stars toward the brighter part, supporting the effectiveness of this technique. A high membership probability extends down to $G \sim 19$ mag, whereas toward the fainter limits, the probability gradually decreases. A majority of the stars with high membership probability follow a tight distribution in the VPD.

We have also plotted the parallax for all the Gaia sources as a function of G-band magnitude (dots in Figure 4, bottom panel). The respective uncertainties in the parallax values are shown with the error bars. The red

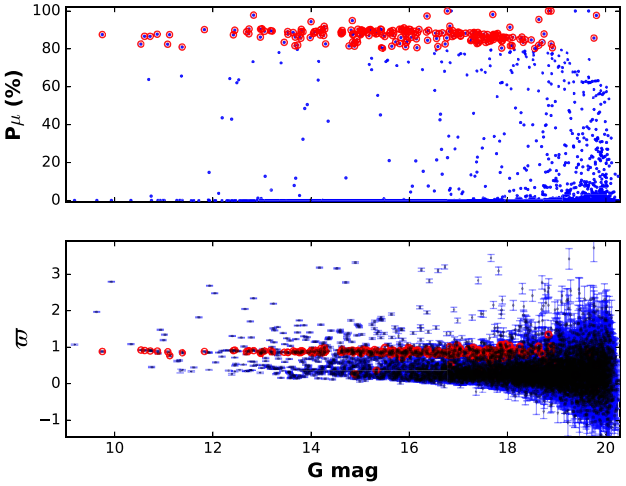

Figure 4. Top panel: Membership probability for the stars located within the cluster area (radius ∼8′) plotted as a function of G-band magnitude. Bottom panel: The blue dots show the distribution of parallax values for the Gaia sources within the cluster as a function of G magnitude. The error bars show respective uncertainties in the parallax values. The red circles represent the probable cluster members ($P_\mu > 70\%$). The green squares represent the probable cluster members with good parallax estimates ($\varpi/\sigma_\varpi > 5$).

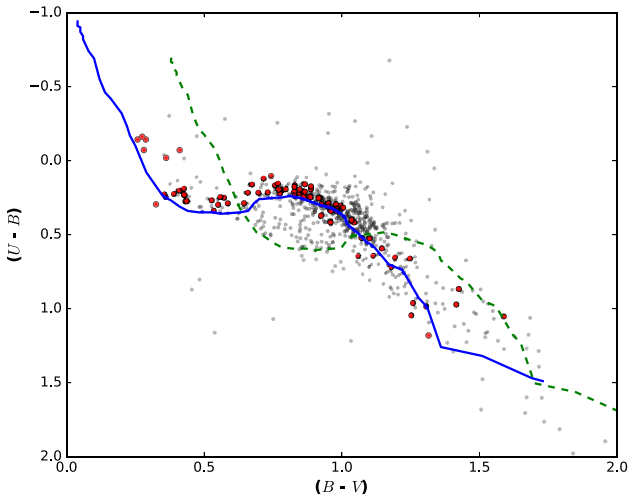

Figure 5. Two color diagram for NGC 1027. Red color circle denotes member stars present within 8 arcmin radius.

circles represent sources having membership probability $P_\mu > 70\%$. We estimate the cluster distance using the parallax values of the cluster members having high membership probability ($P_\mu > 70\%$) and good parallax accuracy ($\varpi/\sigma_\varpi > 5$). These sources are shown with the red circles in Figure 4 (bottom panel). The median parallax value of these sources is 0.892 ± 0.088 mas. We estimate the cluster distance after correcting the median parallax value for the known parallax offset of ~ -0.015 (Stassun & Torres 2021). The distance estimate for the cluster using Gaia data comes out to be $\sim 1.14 \pm 0.11$ kpc, which is in agreement with that reported by Cantat-Gaudin & Anders (2020). Using a matching radius of ∼1 arcsec, we get ∼1610 optical $UBVR_cI_c$ counterparts of Gaia sources with membership probability information within the cluster radius. Out of these, about 160 stars are cluster members.

3.3 *Reddening toward NGC 1027: $(U-B)/(B-V)$ color–color diagram*

Knowledge of reddening is essential for estimation of distance and age of the cluster. The reddening, $E(B-V)$ in the cluster region is determined using the two color diagram (TCD) $(U-B)$ versus $(B-V)$ for the member stars within 8 arcmin (Figure 5). To avoid large uncertainties, we have skipped stars having photometric error >0.1 mag in UBV band. We adopt the slope of the reddening vector $E(U-B)/E(B-V) = 0.72$ and fit the intrinsic zero-age-main sequence (ZAMS) with the solar metallicity (Schmidt-Kaler 1982) for main-sequence stars by shifting the ZAMS for different color excesses. The best fit corresponding to $E(B-V) = 0.36$ mag is shown with the thick curve in Figure 5. The dashed curve shows the ZAMS shifted for a reddening $E(B-V)$ of 0.7 mag. Our estimated value of color excess $E(B-V) = 0.36 \pm 0.04$ mag is comparable to $E(B-V) = 0.41 \pm 0.12$ mag estimated by Maciejewski & Niedzielski (2007). Line-of-sight extinction, A_G, and the reddening, $E(G_{BP}-G_{RP})$, are estimated using the relations given in Wang & Chen (2019). We use $A_G = 1.21$ and $E(G_{BP}-G_{RP}) = 0.35$ for the further analyses of Gaia EDR3 data.

3.4 *Age and distance of the cluster*

The CMDs are important tools to estimate the cluster's age and distance. We have constructed the optical CMDs using cluster members from our optical catalog and Gaia data. V versus $(B-V)$ and V versus $(V-I)$ color–magnitude diagrams for the sources in the cluster region (black dots) along with the member stars (red circles) shown in Figure 6. Figure 7 is plotted using the cluster members with membership probabilities $P_\mu > 70\%$. The CMDs of target cluster show a well-defined narrow main sequence (MS) that extends from $V \sim 10.5$ mag to $V \sim 20$ mag. It is seen that the field star contamination becomes more evident for stars $V \geq 17$ mag.

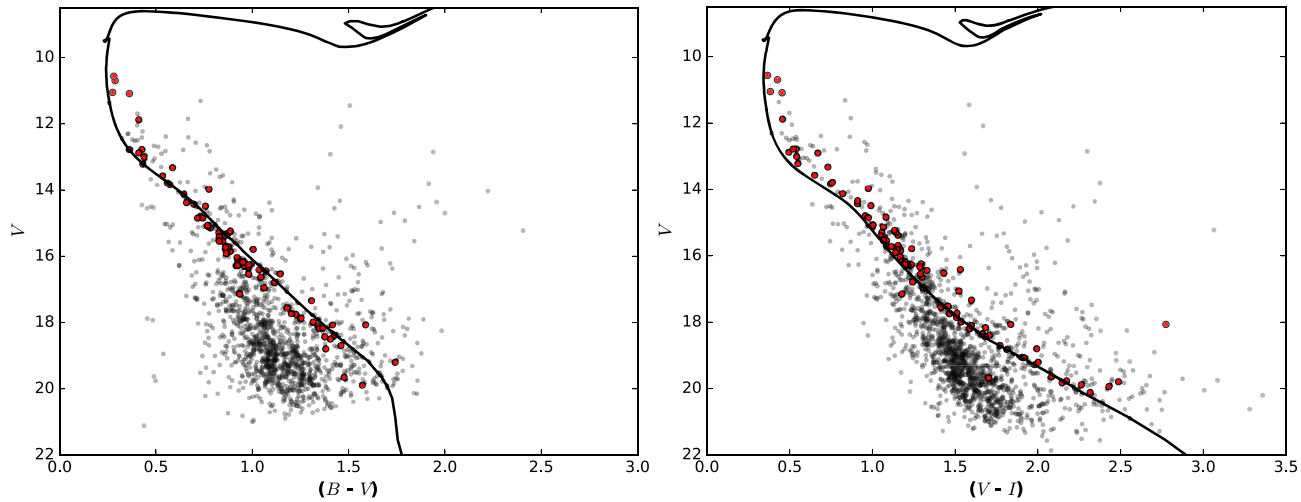

Figure 6. $V/(B-V)$ (left panel) and $V/(V-I)$ (right panel) color magnitude diagrams for the stars in the cluster NGC 1027 (radius ≤8 arcmin). The red circles represent high membership probability members from Gaia EDR3.

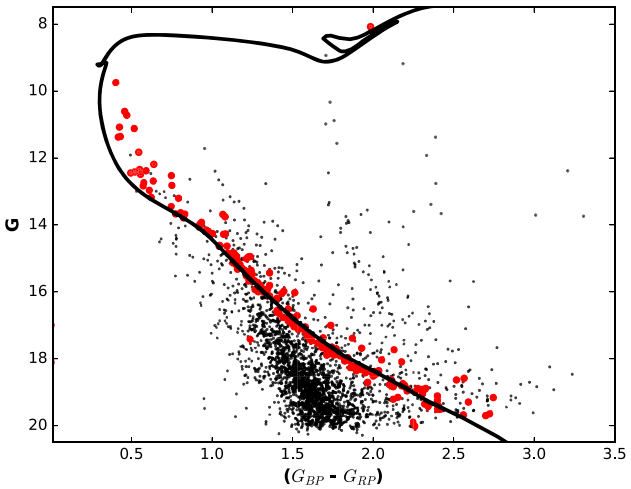

Figure 7. $G/(G_{\rm BP}-G_{\rm RP})$ color–magnitude diagram for the stars in the cluster region. The red circles represent Gaia sources with $P_\mu > 70$. The thick curve represent the main sequence isochrone (Padova–Parsec) for log age of 8.11 corrected for the adopted distance and reddening.

Distance and age estimations of the cluster have been derived by using MS isochrone for solar metallicity taken from Padova PARSEC version 1.2S database of stellar evolutionary tracks and isochrones of Pastorelli *et al.* (2020). This is corrected for the derived reddening values from the TCD. We tried to fit the MS isochrones of different ages over the member stars (shown with the red circles in Figures 6 and 7). The visual best fit of the MS to the blue part of the intrinsic CMDs gives distance modulus $(V-M_V)$. The best fit isochrone yield a distance modulus $(V-M_V)=10.28$ mag indicating a distance of ∼1.14 Kpc for the cluster and a log age of 8.11 (∼130 Myr) corrected for the adopted distance and reddening. Our estimated distance for the target field is comparable to the value of 1.03 Kpc, whereas the age estimation is lower than the value 252 Myr derived by Maciejewski & Niedzielski (2007).

3.5 *Luminosity and mass functions*

Stellar mass cannot be measured directly. Stellar models are required to transform magnitude of a star in a given wavelength into masses. With the help of CMDs, we derive luminosity function (LF) of probable main sequence cluster members and MF using mass–luminosity relation from theoretical evolutionary models. We have used Gaia EDR3 high membership probability members to determine LFs for the cluster. We have used G versus $(G_{\rm BP}-G_{\rm RP})$ CMD to construct the LF. Field star contamination and membership uncertainty affect luminosity and mass function of open star clusters (Scalo 1998). Therefore, to avoid the contribution of the field stars in our sample of cluster members, we have used only kinematic and photometric confirmed members of the cluster for the LF and MF estimations. To determine the completeness of the data, we constructed the magnitude histogram method (Panwar *et al.* 2017). Using the magnitude histogram, we found that completeness of the data limits to $G\sim 18.5$ mag. For estimation of LF, magnitude of the MS stars were converted to absolute magnitude using estimated distance modulus and reddening. Conversion of LF into the present day MF is done using the latest version of theoretical isochrones of Padova's stellar evolutionary tracks and isochrones (Pastorelli *et al.* 2020). To construct MF, we have converted absolute mag bins to mass

bins. Consequently, we transform the LF to MF for all the main-sequence stars (∼180 stars) having mass $0.55 \leq M/M_{\odot} \leq 2.1$. MF slope is given by using a power-law:

$$\Gamma = d\log N(\log m)/d\log m, \quad (3)$$

where $N(\log m)$ is the number of stars per unit logarithmic mass interval. dN is the probable cluster members in a mass bin dM with central mass M. Observational results suggest that the MF slopes is similar to that given by Salpeter (1955), i.e., $\Gamma = -1.35$. The resulting mass function for our target cluster is shown in Figure 8. For the cluster NGC 1027, we obtain the mass distribution, which has a best-fitting slope $\Gamma = -1.46 \pm 0.15$, similar to the Salpeter value.

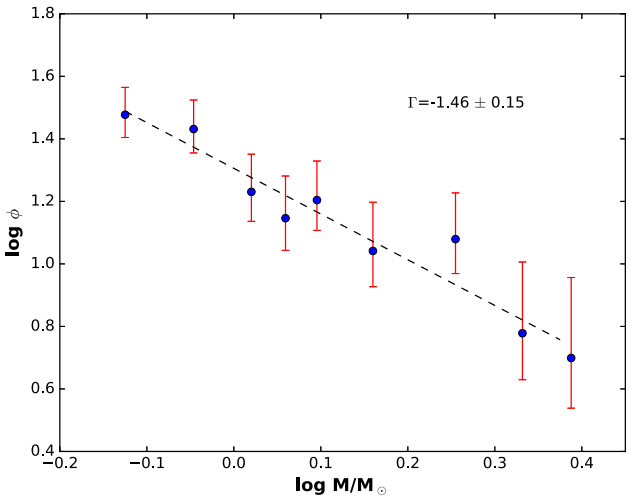

Figure 8. Mass functions of stars using probable member main-sequence stars. The error bars represent $1/\sqrt{N}$.

4. Discussion

Observational investigation of the OCs reveal that in general, massive stars are concentrated toward the nucleus in comparison to low-mass stars, which are mostly distributed in the corona region of the cluster (Soderblom *et al.* 1998; Sharma *et al.* 2000).

This segregation of massive stars toward cluster's center can happen due to the equipartition of energy (dynamical evolution) or due to the star formation processes itself.

We have analysed the radial distribution of probable member stars (with membership probability >70%) in two mass bins, i.e., stars with masses <1.2 $M_{\odot}$ and ≥1.2 $M_{\odot}$, to look for mass segregation effect in NGC 1027 (cf. Figure 9 (left panel)). The distribution clearly demonstrates that stars in the mass bin with massive stars (≥1.2 $M_{\odot}$) are concentrated towards the cluster center compared to low mass stars (mass bin <1.2 $M_{\odot}$), suggesting mass segregation effect in the NGC 1027 cluster. To investigate whether the mass segregation in this cluster is due to star formation processes or due to dynamical relaxation, we estimated the dynamical relaxation time (T_E), i.e., time in which the individual star exchange sufficient energy to achieve the velocity distribution of a Maxwellian equilibrium. We have used

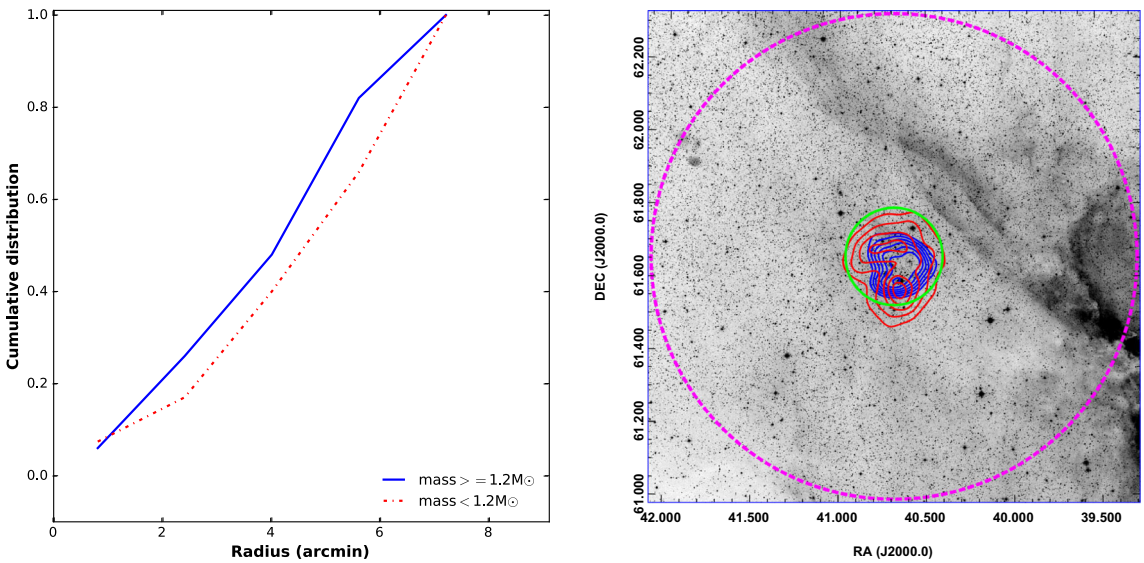

Figure 9. Left panel: Normalized cumulative radial distribution of the member stars in the cluster region. Right panel: DSS2-R image of the open cluster NGC 1027. The red and blue contours show the density distribution of low-mass (<1.2 $M_{\odot}$) and relatively higher-mass (≥1.2 $M_{\odot}$) members, respectively. The green circle shows the cluster radius and magenta dashed circle represents the area (radius ∼40 arcmin), used for the search of kinematic members outside cluster radius.

the method given by Binney & Tremaine (1987) to estimate the dynamical relaxation time (T_E), i.e.,

$$T_E = \frac{N}{8 \log N} \times T_{\rm cross}, \quad (4)$$

where $T_{\rm cross} = D/\sigma_V$ is the crossing time, N is the total number of stars in the cluster region of diameter D and σ_V is the velocity dispersion, with a typical value of 3 km s^{-1} (Bisht *et al.* 2017; Sharma *et al.* 2020). Using the above equation, we estimated the value of T_E as ∼10 Myr for the NGC 1027 cluster. Comparing the cluster age (∼130 Myr) with its dynamical relaxation time (∼10 Myr), we found that the cluster is dynamically relaxed and the observed mass segregation is due to the result of dynamical evolution.

Due to the mass segregation process, low-mass members may become more vulnerable for evaporation and hence, ejected out of the cluster more easily (e.g., see Mathieu 1984). This stellar evaporation results in a continuous decrease of the total mass of the cluster, and hence, the gravitational binding energy of the cluster. However, external disturbances, e.g., the tidal force from nearby giant molecular clouds or star clusters, passages through Galactic spiral arms or disks, or a shear force by Galactic differential rotation, increase the stellar evaporation of the cluster. For a cluster, the tidal radius is defined as a distance at which two gravitational forces; one towards the Galactic center and another toward the cluster center; balances. Thus, tidal radius is estimated to separate gravitationally bound and unbound stars to a cluster. The tidal radius of a star cluster in the solar neighborhood is given by the equation:

$$r_t = \left[\frac{G M_C}{2(A-B)^2}\right]^{1/3}, \quad (5)$$

where G is the gravitational constant, M_C is the total mass of the cluster and A, B are the Oort constants, where $A = 15.3 \pm 0.4$ km s^{-1} kpc^{-1}, $B = -11.9 \pm 0.4$ km s^{-1} kpc^{-1} (Bovy 2017). For the total cloud mass of ∼164 $M_\odot$ estimated from the MF distribution, the corresponding tidal radius is ∼7.8 pc. If we assume that ∼50% of the cluster mass is missed due to data incompleteness, the tidal radius will be ∼9 pc. Therefore, the tidal radius of the cluster is much larger than the present estimate of the cluster radius ($R_{cl} \sim 2.65$ pc), or in other words, this cluster is already started to loose its low-mass members due to dynamics.

Thus, there is a possibility of finding member stars beyond the observed cluster boundary. For this, we searched for the stars sharing the similar proper motion and distance as cluster members, outside the observed cluster boundary.

We estimated the membership probability and found ∼460 stars with membership probability >70% up to a radius of 40 arcmin (cf. Figure 9, right panel).

To study the cluster dynamics and mass segregation, we divided these stars into two mass bins, stars having mass <1.2 $M_\odot$ and stars having mass >1.2 $M_\odot$, and created the respective stellar density distribution maps. The stellar density distributions for above two mass bins are over-plotted on a DSS2-R band image shown in Figure 9 (right panel).

There is a clear evidence of mass segregation as the stars having mass >1.2 $M_\odot$ are concentrated toward the center compared to the relatively low-mass stars.

The spatial distribution of the low mass members in the cluster NGC 1027 show slightly tailed structure (cf. Figure 9, right panel). This might have caused due to the tidal striping of member stars from the cluster. Tidal striping of stars can happen in a cluster due to the tidal forces from a nearby massive object, disk crossing, or differential rotation of the Galaxy. Thus, the tidal stripping depends on the mass and age of a cluster. The ratio of the number of cluster inside the tidal radius to those outside, can tell us about the amount of tidal stripping already done in a cluster. For example, for Blanco 1 (age ∼100 Myr) cluster, it is found to be ∼3 (Zhang *et al.* 2020), whereas for Coma Berenicesa cluster (age ∼700 Myr) this ratio is estimated as 0.6 (Tang *et al.* 2019). However, in case of an old massive star cluster, Hyades (age ∼800 Myr), this ratio is estimated as ∼1.1 (Röser *et al.* 2019). NGC 1027 is relatively young and appears to be more dynamically bound. The observed radius of the cluster suggest that it is a dynamically relaxed cluster that show mass-segregation and has already lost some of its member stars and currently, it is in the process of dissolution due to the influence of external tidal interactions.

5. Summary and conclusion

We present the photmetric and kinematic studies of the intermediate age open cluster NGC 1027 using $UBVRI_c$ data taken with 1.04-m Sampunanand telescope and Gaia EDR3 data. The results of the study are summarized as follows:

1. Using two-dimensional KDEs analysis of the Gaia EDR3 data, we have obtained the cluster center i.e., about 4 arcmin away from the center mentioned in

WEBDA. The cluster extent is estimated to be about 8.0 arcmin.

2. The distribution of proper motion of the stars in the cluster region shows a clear separation between the cluster members and field stars. The mean proper motion for the cluster has been estimated to be $(\mu^{\star}_{\alpha}, \mu_{\delta}) = (-0.84, 2.04)$ mas yr^{-1}.
3. Based on the membership analysis, 217 member stars are identified ($P_{\mu} > 70\%$) in the cluster region. Their mean parallax value is 0.892 ± 0.088 mas corresponding to a distance of $\sim$1.14 kpc.
4. The $(U - B)/(B - V)$ color–color diagram for the cluster members give a reddening $E(B - V) \sim 0.36 \pm 0.04$ mag towards the cluster.
5. The CMDs for the cluster members, constructed using *UBVRI* photometric data and Gaia EDR3 data, show that NGC 1027 is an intermediate age OC with an age $\sim$130 Myr and located at a distance of $\sim$1.14 kpc.
6. The LFs and MFs are determined by considering the members selected from Gaia proper motion database and photometry. The mass function slope for the cluster, $\Gamma = -1.46 \pm 0.15$, is in good agreement with that given by Salpeter (1955) for the Galactic OCs.
7. We have studied the radial distribution of stellar masses within the cluster region and found that relatively massive stars are dominantly distributed in the inner regions of the cluster suggesting mass segregation.
8. We reported the presence of astrometric members of the target field outside the clusters radius. The observed small size of the cluster when compared to its tidal radius, indicates mass-segregation, slightly elongated morphology and a comparison of dynamical relaxation time with the age of cluster. We conclude that the cluster is under the influence of external tidal interactions.

Acknowledgements

We are thankful to anonymous referee for providing the comments that significantly improve the manuscript. NP acknowledges the financial support received through the SERB CRG/2021/005876 grant. This research has made use of the WEBDA database, operated at the Department of Theoretical Physics and Astrophysics of the Masaryk University. This work has made use of data from the European Space Agency (ESA) mission Gaia https://www.cosmos.esa.int/gaia), processed by the Gaia. Data Processing and Analysis Consortium. AT also like to acknowledge Prof. U. S. Pandey for his scientific suggestions and corrections.

References

Angelo M. S., Piatti A. E., Dias W. S., Maia F. F. S. 2019, MNRAS 488, 1635
Bastian N., Covey K. R., Meyer M. R. 2010, arXiv:1001.2965
Bate M. R., Bonnell I. A., Bromm V. 2003, MNRAS 339, 577
Binney J., Tremaine S. 1987, Galacric dynamics (Princeton, NJ: Princeton University Press)
Bisht D., Yadav R., Durgapal A. 2017, New Astronomy 52, 55
Bisht D., Yadav R., Ganesh S. *et al*. 2019, MNRAS 482, 1471
Bostancı Z. F., Yontan T., Bilir S. *et al*. 2018, Astrophysics and Space Science 363, 143
Bovy J. 2017, MNRAS 468, L63
Cantat-Gaudin T., Anders F. 2019, VizieR Online Data Catalog J/A+A/633/A99
Cantat-Gaudin T., Anders F. 2020, A&A 633, A99
Cantat-Gaudin T., Jordi C., Vallenari A. *et al*. 2018, A&A 618, A93
Carraro G., Costa E. 2007, A&A 464, 573
Carraro G., Vázquez R. A., Moitinho A. 2008, A&A 482, 777
Castro-Ginard A., Jordi C., Luri X. *et al*. 2018, A&A 618, A59
Castro-Ginard A., Jordi C., Luri X. *et al*. 2020, A&A 635, A45
Chauhan N., Pandey A. K., Ogura K. *et al*. 2011, MNRAS 415, 1202
Chen L., Hou J. L., Wang J. J. 2003, AJ 125, 1397
Dib S., Schmeja S., Hony S. 2017, MNRAS 464, 1738
Elmegreen B. G. 2000, ApJ 530, 277
Friel E. D. 1995, ARA&A 33, 381
Gaia Collaboration 2020, VizieR Online Data Catalog, I/350
Gaia Collaboration, Helmi A., van Leeuwen F., *et al.* 2018, AAP 616, A12
Gao X.-H. 2014, Research in Astronomy and Astrophysics 14, 159
Girard T. M., Grundy W. M., López C. E., van Altena W. F. 1989, AJ 98, 227
Harris W. E., Pudritz R. E. 1994, ApJ 429, 177
Joshi Y. C., Dambis A., Pandey A. K., Joshi S. 2016, A&A 593, A116
Joshi Y. C., Maurya J., John A. A. *et al*. 2020, MNRAS 492, 3602
Kharchenko N., Piskunov A., Schilbach E., Röser S., Scholz R.-D. 2013, A&A 558, A53
King I. 1962, AJ 67, 471
Kroupa P. 2002, Science 295, 82
Lada C. J., Lada E. A. 2003, ARA&A 41, 57
Landolt A. U. 1992, AJ 104, 340
Liu L., Pang X. 2019, ApJSS 245, 32

Maciejewski G., Niedzielski A. 2007, A&A 467, 1065
Mathieu R. D. 1984, ApJ 284, 643
Medhi B. J., Tamura M. 2013, MNRAS 430, 1334
Miholics M., Webb J. J., Sills A. 2014, MNRAS 445, 2872
Pandey R., Sharma S., Panwar N. *et al*. 2020, ApJ 891, 81
Pang X., Li Y., Tang S.-Y., Pasquato M., Kouwenhoven M. 2020, ApJL 900, L4
Panwar N., Samal M., Pandey A. *et al*. 2017, MNRAS 468, 2684
Pastorelli G., Marigo P., Girardi L., *et al*. 2020, MNRAS 498, 3283
Phelps R. L., Janes K. A. 1994, ApJSS 90, 31
Röser S., Schilbach E., Goldman B. 2019, A&A 621, L2
Ruprecht J. 1966, Bulletin of the Astronomical Institute of Czechoslovakia 17, 98
Sagar R., Piskunov A., Miakutin V., Joshi U. 1986, MNRAS 220, 383
Salpeter E. E. 1955, ApJ 121, 161
Scalo J. 1998, The Stellar Initial Mass Function (38th Herstmonceux Conference), Vol. 142, p. 201
Schmidt-Kaler T. 1982, A&A 19
Sharma A. K., Tuzla K., Matsen J., Chen J. C. 2000, Powder Technology 111, 114
Sharma S., Ghosh A., Ojha D. K. *et al*. 2020, MNRAS 498, 2309
Soderblom D. R., King J. R., Hanson R. B. *et al*. 1998, ApJ 504, 192
Stassun K. G., Torres G. 2021, ApJL 907, L33
Stetson P. B. 1987, PASP 99, 191
Stetson P. B. 2000, Publications of the ASP 112, 925
Tang S.-Y., Pang X., Yuan Z., *et al*. 2019, ApJ 877, 12
Tripathi A., Pandey U. S., Kumar B. 2014, New Astronomy 29, 1
Trumpler R. J. 1930, Lick Observatory Bulletin 420, 154
Wang S., Chen X. 2019, ApJ 877, 116
Yadav R. K. S., Sariya D. P., Sagar R. 2013, MNRAS 430, 3350
Zhang Y., Tang S.-Y., Chen W. P., Pang X., Liu J. Z. 2020, ApJ 889, 99